High-Resolution Metabolic Mapping of the Cerebellum Using 2D Zoom Magnetic Resonance Spectroscopic Imaging

Uzay E. Emir[1,2*], Jaiyta Sood[1], Mark Chiew[3], Albert Thomas[4], Sean P. Lane[5]
[1]School of Health Sciences, Purdue University, West Lafayette, Indiana
[2]Weldon School of Biomedical Engineering, Purdue University, West Lafayette, Indiana
[3]Wellcome Centre for Integrative Neuroimaging, University of Oxford, UK
[4]Department of Radiology, University of California Los Angeles, Los Angeles, California
[5]Department of Psychological Sciences, Purdue University
*Corresponding Author

Correspondence:
Uzay Emir, School of Health Sciences, Purdue University, School of Health Sciences,
550 Stadium Mall Drive, West Lafayette, IN 47907.
Email: uemir@purdue.edu

Data Availability Statement

The data that support the findings of this study are available from the corresponding author upon reasonable request.

Funding Statement

The study was supported by the Indiana CTSI and funded in part by grant #UL1TR001108 from the NIH, NCATS, CTS Award

Conflict of Interest Disclosure

Authors declare that they have no conflict of interest.

Ethics Approval Statement

The study was conducted in accordance with the institutional review board of Purdue University.

Patient Consent Statement

Before being scanned, an informed written assent was obtained from all the subjects.

The Short Running Title

Reduced field of View Magnetic Resonance Spectroscopic Imaging

Word count: 3108

Abstract

Purpose: The human cerebellum plays an important role in the functional activity of the cerebrum, ranging from motor to cognitive systems given its relaying role between the spinal cord and cerebrum. The cerebellum poses many challenges to magnetic resonance spectroscopic imaging (MRSI) due to its caudal location, susceptibility to physiological artifacts, and partial volume artifacts resulting from its complex anatomical structure. Thus, in the present study, we propose a high-resolution MRSI acquisition scheme for the cerebellum.

Methods: A zoom or reduced-field of view (rFOV) metabolite-cycled MRSI acquisition at 3T, with a grid of 48 × 48, was developed to achieve a nominal resolution of 62.5 μL. Single-slice rFOV MRSI data were acquired from the cerebellum of 5 healthy subjects with a nominal resolution of $2.5 \times 2.5 \times 10$ mm^3 in 9. 6 minutes. Spectra were quantified using the LCModel package. A spatially unbiased atlas template of the cerebellum was used to analyze metabolite distributions in the cerebellum.

Results: The superior quality of the achieved spectra enabled generation of high-resolution metabolic maps of total N-acetylaspartate, total creatine, total choline, glutamate+glutamine, and myo-inositol, with Cramér-Rao lower bounds below 50%. A template-based regions of interest (ROI) analysis resulted in spatially dependent metabolite distributions in 9 ROIs. The group- averaged high-resolution metabolite maps across subjects increased the contrast-to-noise ratio between cerebellum regions.

Conclusion: These findings indicate that very high-resolution metabolite probing of the cerebellum is feasible using rFOV or zoomed MRSI at 3T.

Keywords: cerebellum, metabolic map, reduced field of view, spectroscopic imaging, concentric rings

Abbreviations: 2D, two dimensional; ANOVA, analysis of variance; CRLB, Cramér-Rao lower bound; CRT, concentric ring trajectory; DW, density weighted; FID, free induction decay; FOV, field of view; GABA, γ-aminobutyric acid; Gln, glutamine; Glu, glutamate; GPC, glycerophosphocholine; GRESHIM, gradient-echo shimming; GSH, glutathione; HLSVD, Hankel-Lanczos singular value decomposition; Lac, lactate; MNI, Montreal Neurological Institute; MRSI, magnetic resonance spectroscopic imaging; myo-Ins, myo-inositol; NAA, N-acetylaspartate; NAAG, N-acetylaspartylglutamate; PCho, phosphocholine; PCr, phosphocreatine; rFOV, reduced field of view; SAR, specific absorption rate; SBW, spectral bandwidth; SD, standard deviation; semi-LASER, semi-localization by adiabatic selective refocusing; SNR, signal-to-noise ratio; spatially unbiased atlas template, SUIT; tCho, total choline; tCr, total creatine; UHF, Ultra High-Field; VOI, volume of interest

Introduction

Compared to the cerebrum, the cerebellum constitutes only 10% of total brain volume, however it has 3 times more neurons than the cerebrum (1), and consumes around 20% of the whole energy utilization of the brain (2). The human cerebellum plays an important role in functional activity of the brain, which ranges from motor to cognitive systems, due to its relaying role between the spinal cord and cerebrum. With the development of neuroimaging modalities, the cerebellum has been a focus of interest, but its complex structure and caudal location poses technical challenges for imaging modalities (3). Increasingly, advanced MRI technologies including anatomical and functional modalities have facilitated the evaluation of the cerebellum (4,5). This is of great importance since abnormalities in the cerebellum are associated with many neurological, neurodevelopmental, and psychiatric disorders (6–9).

Magnetic resonance spectroscopy (MRS) techniques are increasingly used to enable the neurochemical probing of brain tissue (10). Single voxel (SV) MRS has been the method of choice to study the cerebellum with a nominal voxel dimension ranging from 4090 μL (11) to 15620 μL (12) for different neurological conditions. However, spectra in single SV-MRS acquisitions are derived from a mixture of different tissue compartments, which results in a partial volume effect. This partial volume effect is particularly problematic in the cerebellum due to its complex structures.

Alternatively, MRS imaging (MRSI) methods record multiple spectra from different regions simultaneously. The widespread use of MRSI has been limited by several challenges, including low signal-to-noise ratio (SNR) due to suboptimal sequences, inhomogeneity of the main (B0) and radiofrequency (B1) magnetic fields, and long acquisition times (13). As increasingly advanced MRI acquisition and reconstruction approaches have been developed, sensitivity and resolution of MRSI has drastically improved. Recently, a nominal resolution of 110 μL has been reported for 3D-MRSI of the whole-cerebrum at 3T (14). Further improvements in resolution up to 36 μL have been reported with the use of constrained reconstruction of 3D-MRSI at 3T (15). Simultaneously, efforts at Ultra-

High-Field (UHF≥7T) MRI have resulted in further improvements in resolution both for 2D and 3D MRSI. A nominal resolution of 24 μL with an acquisition duration of 46 minutes has been reported at 9.4T using 2D MRSI (16). As for the 3D-MRSI, a nominal resolution of 20 μL has been achieved within 17 minutes at 7T (17). Although there have been numerous achievements for neurochemical mapping cerebrum using MRSI both at 3T and UHF, the cerebellum has not been a focus of interest due to the caudal location and the susceptibility to physiological artefacts. Only very few studies have been performed using ^{1}H MRSI in the cerebellum with coarse nominal resolutions ranging from 310 μL (18) to 1210 μL (19).

Zoom-MRI or reduced-field of view (rFOV) acquisition schemes overcome the limitations of spatial resolution and low signal to noise ratio (SNR) for MRI. This has been achieved by using outer volume suppression (OVS) (20) or a well-defined spatial excitation (21). Similar to Zoom-MRI, three-pulse localization of MRSI suppresses the signal outside of the FOV and is used for rFOV MRSI measurements to reduce acquisition duration by reducing the number of phase encoding steps (22,23). In contrast to previous rFOV MRSI implementations, the present study sought to develop an accelerated rFOV acquisition scheme without reducing phase encoding steps for high-resolution short echo-time (TE) semi-LASER MRSI at 3T with a nominal resolution of 62.5 μL. In order to increase the SNR of the zoomed acquisition, k-space data was acquired with a sampling density proportional to a Hanning window (24). Further SNR gain was achieved using a narrower acquisition bandwidth. In five healthy subjects, we demonstrated that the proposed rFOV-MRSI with accelerated k-space trajectory generates high-resolution metabolic maps at 3 Tesla across an entire cerebellum slice with a thickness of 10 mm. Finally, we explored neurochemical alterations in regions of interest (ROIs) of the cerebellum using the spatially unbiased atlas template of the cerebellum (SUIT Atlas) (4).

Methods

Five healthy subjects [three females, 25.5 ± 7.07 years (mean ± std)] participated. All subjects provided informed consent before the in-vivo MRI exam which was approved by the Purdue University institutional review board.

MRI data acquisition

The data were acquired using a Siemens Prisma 3T MR system (Siemens, Germany) with a 64-channel ($N_{channels}$) head array receive coil. A T1-weighted MP-RAGE dataset (TR = 1900 ms, TE = 2.13 ms, TI = 900 ms, flip angle = 8°, 176 transverse slices, 0.9 x 0.9 x 1 mm^3 voxels) was acquired for each subject for MRSI acquisition planning. B0 shimming was achieved by using the vendor-provided procedure, GRESHIM (gradient-echo shimming). The vendor-provided “patient-specific" B1 shimming option was used.

Reduced field of view, Zoomed, metabolite-cycled semi-laser MRSI

Metabolite-cycling MRSI was acquired by using the same parameters as described in Emir et al. (25). Briefly, before the semi-LASER localization, two asymmetric inversion RF pulses in alternating TRs were used for downfield/upfield ($N_{directions}$ = 2 [upfield/downfield]) measurements.

The semi-LASER localization (Figure 1A and Supporting Information Figure S1) was positioned in the central cerebellar slice in the transverse plane without any angulation, to include Right Crus I, Left Crus I, and Dentate Nuclei (Figure 1B). The high in-plane nominal resolution (2.5 mm × 2.5 mm) with a thickness 10 mm was achieved using rFOV = 120 mm × 120 mm × 10 mm, semi-LASER localization = 100-90 mm × 50-40 mm × 10 mm, TR = 1500 ms, and TE = 32 ms. The semi-LASER volume of interest (VOI) was placed asymmetrical in the rFOV.

To cover the 48 x 48 grid in a rFOV, we modified our 2D-density weighted concentric ring trajectory (DW-CRT) design (24). Each ring in DW-CRT consisting of 64 points (number of points per ring, N_{p_ring} = 64) was collected with an ADC bandwidth of 40 kHz. This resulted in 128 spectral points (N_{sp} = 128). Two temporal interleaves (number of temporal interleaves, N_{ti} = 2) with inverted readout gradients were collected with an SBW of 625 Hz (24). The total acquisition window was 205 ms for 256 spectral points. The rest of the DW-CRT parameters were identical to the previous 3T and 7T implementations (24,26):

four spatial interleaves (N_{si} = 4 and N_{avg} = 1) of 24 DW concentric rings (N_{ring} = 24) were acquired with α = 1. The total duration for the DW-CRT was 9 minutes 36 seconds ((N_{si} = 4) x ($N_{directions}$ = 2) x (N_{ring} = 24) x (N_{ti} = 2) x (TR = 1500 ms) = 576 seconds).

Post processing

MATLAB (MathWorks, Natick, MA, USA) was used for reconstruction. To achieve the full SBW (1250 Hz), NUFFT (27) was used to calculate the Fourier transform of the acquired k-space data (24). The metabolite-cycled spectra were processed as described in Emir, et al. (25). A Gaussian filter of 250-ms timing parameter were applied to the FIDs. The non-water-suppressed spectra enabled frequency and phase corrections for each voxel with a dimension of 62.5 μL. The metabolite spectra were obtained via subtracting the upfield and downfield FIDs, while summing them generated the water-only spectra. The remaining water signal in the metabolite spectrum was removed using the Hankel-Lanczos singular value decomposition (28). A lipid-basis penalty algorithm was used to minimize the lipid contamination (29). Water-only and metabolite-only whole cerebellum slice images were used to generate a brain and lipid mask for the lipid-basis penalty algorithm.

Metabolite Quantification

Metabolite quantification was performed using LCModel package (30). The model spectra including eight LCModel-simulated macromolecule resonances (positioned at 0.91, 1.21, 1.43, 1.67, 1.95, 2.08, 2.25, and 3 ppm) was used as a basis-set for the LCModel analysis, as described in Emir, et al. (26). The basis-set included the model spectra of alanine (Ala), aspartate (Asp), ascorbate/vitamin C (Asc), glycerophosphocholine (GPC), phosphocholine (PC), creatine (Cr), phosphocreatine (PCr), GABA, glucose (Glc), glutamine (Gln), glutamate (Glu), glutathione (GSH), lactate (Lac), myo-Inositol (myo-Ins), N-acetylaspartate (NAA), N-acetylaspartylglutamate, phosphoethanolamine (PE), scyllo-Inositol (scyllo-Ins), and taurine (Tau). The LCModel fitting was performed over the spectral range from 0.5 to 4.2 ppm. The resulting Cramér-Rao lower bounds of estimated metabolites less than 50 % were reported. Summed metabolite estimations were reported for total NAA (NAA+NAAG, tNAA), total Cr (Cr + PCr, tCr), total choline (GPC + PC, tCho) and Glu and Gln (Glu + Gln, Glx), since their pairwise-correlation estimates were high (correlation coefficient < −0.5). The normalized metabolite levels were reported for each subject using the water-scaled signal intensity of each metabolite (raw): Metabolite-normalized=Metabolite-raw/($tCho_{raw}$+tCr_{raw}+$tNAA_{raw}$+*myo*-Ins_{raw}+Glx_{raw}).

Metabolite levels were also reported using water scaling and relative to tCr approaches. These metabolite levels were not corrected for T_1 andT_2 effects, partial volume and water content differences.

Regional Distributions of Neurochemical in the Cerebellum

The Cerebellar ROIs were obtained using the Cerebellar MNI FNIRT Maxprob thr25-2mm of SUIT Atlas (http://www.diedrichsenlab.org/imaging/propatlas.htm). Each subject’s MRSI slice and metabolite maps was determined in the MP-RAGE image space using SPM (31). The resulting MRSI resolution was 0.9 x 0.9 x 1 mm^3. Then, ROIs of the SUIT atlas were warped into each subject’s MP-RAGE image space in the following manner (Supporting Information Figure S2): each subject's MP-RAGE image was nonlinearly registered to the Montreal Neurological Institute-152 template by using the FMRIB Nonlinear Registration Tool (FNIRT); afterwards, the resulting warp field was applied to the Cerebellar MNI FNIRT Maxprob thr25-2mm of the SUIT atlas to transform them to each subject's MPRAGE image. Mean metabolite levels in cerebellar ROIs were calculated using fslstats (32) in the center slice of MRSI in the transverse plane.

To generate group-averaged metabolite spatial maps, metabolite maps were transformed to the MNI-152 template by applying the resulting warp field; afterwards metabolite maps were averaged across the five subjects.

Statistical Analysis

Only the ROIs that were consistently detected across subjects (in at least half of the subjects), were included in statistical analyses. As a secondary filter to select reliable ROIs, the mean number of voxels in each ROIs had to be one standard deviation above the mean standard deviation.

The mean regional metabolite-normalized levels from the aforementioned reliable ROIs of cerebellar atlas were used for statistical analyses using SAS software v.9.4 (SAS Institute, Cary, NC, 2014). MRS data from different ROIs were compared using a one-way repeated measures analysis of variance separately for each reported normalized metabolites (tNAA, tCr, tCho, Glx and *myo*-Ins) across each target brain region (within-subject factor). Given the occurrence of missing data due to exclusion for unreliability, we utilized restricted maximum likelihood to fit the models. Each analysis examined the differences in MRS data across 9 ROIs, resulting in 36 possible pairwise comparisons. We employed a Benjamini-Hochberg correction within each family of comparisons in order to control the false discovery rate (33). The same statistical analysis was performed for the water scaled and relative to tCr approaches.

Results

Figure 1A shows coronal, sagittal, and axial images of an anatomical scan including the placement of the MRSI slice and semi-LASER localization. The image derived from the non-water suppressed MRSI data shows the signals from the cerebellum. ROIs of the SUIT atlas encompassed by the MRSI localization are illustrated in Figure 1B. The list of ROIs and the mean number of voxels for each metabolite that met our criteria for reliable quantification in the SUIT atlas are listed in Table 1.

Figure 2A and 2B show the zoomed MRSI spectra with LCModel fits. Even at a nominal resolution of 62.5 μL at 3T, spectra from five different volumes of interest are of high quality enough for reliable quantitation. Although LCModel-simulated macromolecule resonances account for most of residual lipid signal in the spectral range of 0.5-1.8 ppm, some voxels have negative peaks at 1.8 ppm (gray box in Figure 2B) due to regularization error of the L2 lipid removal procedure.

The mean CRLB values for each ROI across subjects are reported in Table 2. In most of the voxels, the mean CRLB values after the Gaussian filter resulted in values less than 30% for the metabolites tNAA, tCr, tCho, myo-Ins, and Glx. The resulting normalized metabolite maps and corresponding CRLB maps of a healthy subject are illustrated in Figure 3A and Figure 3B, respectively.

Figure 4 shows the group-average metabolite maps of normalized metabolite levels in the MNI-152 template space. The mean normalized metabolite levels that met our criteria for reliable quantification in cerebellar ROIs (nine cerebellar ROIs) of the SUIT atlas are shown in Figure 5 (Supporting Information Table S1). The normalized metabolite levels revealed different neurochemical profiles that may characterize different cerebellar regions (Supporting Information Table S4). For instance, the tCho, tNAA, and myo-Ins levels in the Dentate Nuclei are significantly higher than the Right and Left Crus I and Vermis ROIs, whereas tCr is significantly lower compared to the Right and Left Crus I and Vermis ROIs. Similarly, Dentate Nuclei has higher tCho, tNAA, and myo-Ins levels compared to the Vermis ROIs. Similar findings were also observed for water scaled metabolite levels and metabolite ratios (Supporting Information Table S2, S3 for metabolite levels and Table S5 and S6 for statistical findings). However, statistical significance degraded for water scaled metabolite levels (Supporting Information Table S6).

Discussion

This study has demonstrated the advantage of rFOV (zoom) acquisition, zoomed, with a DW-CRT short TE semi-laser localization to improve the resolution and accuracy of whole cerebellum slice metabolic maps at 3T. The improved resolution and spectral quality enabled reliable quantification of tNAA, tCr, tCho, Glx and *myo*-Ins from a nominal voxel volume of 62.5 μL. The metabolite distribution maps for different ROIs in the cerebellum were consistent with the literature (see below). To our knowledge, this is the first study to have demonstrated a higher nominal resolution of 62.5 μL at 3T for the cerebellum.

Implementing the rFOV acquisition at 3T for high-resolution MRSI faces several challenges caused by hardware and signal-to-noise ratio limitations. Mainly, high-resolution MRSI puts demands on maximum gradient amplitudes, rise time, and slew rate. To decrease the field of view while maintaining the acquisition matrix size, one might choose to increase the gradient amplitude and slew rate or to reduce the spectral bandwidth resulting in lower spectral sampling. In this study, to reach the nominal in-plane resolution of 2.5 mm x 2.5 mm, we decided to utilize reduced SBW (625 Hz vs 1250 Hz) compared to previous implementations (26). The SBW was doubled (1250 Hz) using an inverted readout gradient trajectory without causing any additional noise (24). The use of DW-CRT and its reconstruction pipeline further contributed the SNR improvement as discussed previously by Chiew et al. (24). Besides, a lower acquisition bandwidth of 40 kHz compared to the previous implementation of 80 kHz (25,26,34) minimized a larger amount of noise sampled due to the narrower frequency range. Moreover, the 64-ch Head/Neck coil allowed the incremental SNR gains in the peripheral ROIs closest to the coil elements, like the cerebellum (35). Finally, additional SNR improvement was achieved through the use of metabolite-cycling, allowing us voxel-vise preprocessing steps (25).

The present study did not directly compare this acquisition to others at 3 Tesla in which the nominal resolution ranged from 310 μL (18) to 1210 μL (19) for the cerebellum. We believe that our strategy offers substantial resolution improvement for 2D MRSI compared to the other implementations of the cerebrum at 3T and UHF. When the acquisition duration and magnetic field difference were considered, the achieved nominal resolution of 62.5 μL and provided metabolite maps within 9 minutes 36 seconds in the cerebellum are comparable with the 3T and the UHF 2D MRSI in the cerebrum. For instance, a nominal voxel size of 24 μL at 9.4 T (16) and of 29 μL at 7T (36) were achieved with acquisition durations of 46 and 42 minutes, respectively. With the use of constrained reconstruction methods, the proposed strategy is expected to provide higher resolution (15,37).

The rFOV MRSI acquisition with a resolution of 62.5 μL allowed reliable quantification of major brain metabolites in the cerebellum (Figure 2 and 3). Concentration distributions in the cerebellum of the reported metabolites revealed significant variations between the cerebellar vermis, white, and gray matter of both cerebellar hemispheres, and these were in line with previous MRSI and SV-MRS studies. For example, the high cerebellar total creatine level in the gray matter agreed with previous reports (19). In addition, the higher Glx level obtained in cerebellar gray matter was consistent with the previous SV-MRS studies (38). The highest total choline levels were observed in the cerebellar white matter, also in agreement with SV-MRS (38).

The voxel-based comparisons of the SUIT Atlas ROI (4) analyses of whole cerebellum slice metabolite maps demonstrated that metabolite distributions are spatially dependent. The dentate nuclei, the link in the cortico-cerebellar closed loop circuits (39), had higher tNAA, tCho, and myo-ins levels. Since NAA was extensively distributed in the cerebellum and NAAG was very high in the deep cerebellar nuclei, higher tNAA levels observed in the dentate nuclei is in agreement with previous studies (40). Since the dentate nuclei are embedded in the white matter having a higher glia-to-neuron ratio than grey matter (41), myo-inositol and tCho as markers of glial cells resulted in higher levels in the dentate nuclei. In line with the cyto and receptor architectonic mapping of glutamate receptors in the human cerebellum (42), Glx levels were higher in the cerebellar cortex (Right Crus I, Left Crus I and Vermis) than in the dentate nuclei. Finally, higher creatine levels in the cerebellar cortex might suggest energy demand of Purkinje cells (19). With the accurate coregistration between the MRSI and MNI template, high-quality group-average metabolite distributions of tNAA, tCr, tCho, Glx, and myo-Ins were achieved.

The number of subjects is a limitation, and further experiments are required for the clinical validity of the proposed method. In addition, a single slice acquisition is not sufficient to map the entire cerebellum. Although the use of DW-CRT with α=1 resulted in an improved signal-to-noise ratio (24), it deteriorates the point spread function and dilutes metabolite levels in small ROIs like the dentate nuclei. Moreover, limited coverage of the single-slice measurement of zoom MRSI can be overcome using multi-slice stacks with different slice orientations, providing improved coverage and resolution in the cerebellum.(43). The use of a long TR of 1.5 s and the cost of increased total acquisition duration due to the choice of adiabatic pulses can be mitigated by gradient-modulated offset-independent adiabaticity (GOIA) pulses (44). Together with temporal interleaves (N_{ti} = 2) total acquisition was 9 minutes 36 seconds. Recently, we have reduced acquisition duration to 4 minutes 48 seconds by reducing the spectral bandwidth to 893 Hz (Nti = 1) with the use of maximum slew rate of the gradient system (data was not shown). Although multiplet structures can still be resolved with acquisition window of 205 ms (corresponding to a spectral sampling resolution of 5 Hz), maintaining an high spectral sampling resolution is recommended for better separation (45). As in all spectral subtraction-based techniques, the metabolite-cycling technique relies on homogenous B1 and B0 fields for an effective inversion profile. Although it had reported previously that the metabolite-cycling technique resulted in higher metabolite levels compared to the water suppression techniques (25,46), the metabolite signals in the spectral range between 4.2 and 3.8 ppm might be affected by the adiabatic inversion pulses. Thus, further advances in hardware such as multi-transmit and shim coils are expected to improve the performance the metabolite-cycling by providing homogeneous B1 and B0 fields in the cerebellum. Finally, the exact quantification of peaks might be affected by the use of simulated macromolecules and lipid removal procedures.

In conclusion, the rFOV 2D MRSI resulted in very high-resolution metabolite maps of the cerebellum. These initial findings indicate that optimal methods can be developed for the future to generate a probabilistic metabolic atlas of the cerebellum.

Tables

		Mean Number of Voxel ± Standard Deviation				
		tNAA	tCr	tCho	Glx	myo-Ins
ROIs	Dentate Nucleus	150±44	150±44	150±44	131±45	148±41
	Right Crus I	961±89	961±89	926±83	915±109	945±94
	Left Crus I	817±193	817±193	774±191	761±188	794±198
	Right VI	488±181	488±181	484±179	471±176	485±183
	Vermis CRUS II	91±27	91±27	91±27	91±27	91±27
	Vermis. VIIB	45±17	45±17	45±17	45±17	45±17
	Vermis VIIIa	91±7	91±7	91±7	91±7	91±7
	Vermis IX	54±20	54±20	54±20	51±21	54±20
	Vermis X	38±14	38±14	33±16	35±15	38±15

Table 1 The list of ROIs and the mean number of voxels across subjects for each metabolite calculated in the center slice of semi-LASER VOI transformed to MPRAGE

dimensions. The resulted resolution of the center slice was 0.9 x 0.9 mm^2. ROIs are in rows and metabolites are in columns.

		Mean CRLB ± Standard Deviation				
		tNAA	tCr	tCho	Glx	myo-Ins
ROIs	Dentate Nucleus	9.0±1.9	8.3±2.4	10.3±2.0	26.3±8.5	10.0±3.7
	Right Crus I	9.7±1.9	6.4±0.9	11.9±1.7	15.1±1.7	10.8±1.6
	Left Crus I	11.4±1.6	6.7±1.0	13.0±2.5	17.4±3.8	11.3±2.2
	Right VI	7.2±0.8	4.7±1.1	8.7±0.7	12.6±0.9	6.7±0.3
	Vermis CRUS II	6.5±0.3	3.9±0.4	8.4±1.2	9.0±1.2	6.9±1.3
	Vermis. VIIB	6.2±1.2	3.5±0.5	7.2±1.2	11.7±3.1	5.8±0.8
	Vermis VIIIa	7.2±2.2	4.5±0.9	8.3±1.2	12.6±4.5	6.6±1.2
	Vermis IX	11.7±5.0	6.2±1.4	10.7±1.9	18.3±7.6	8.3±1.3
	Vermis X	22.4±7.0	16.25±11.0	29.0±12.2	22.4±9.7	17.0±11.2

Table 2 The list of ROIs and the mean CRLBs across subjects for each metabolite. ROIs are in rows and metabolites are in columns.

Figure Captions

Figure 1 (A) Representative semi-LASER localization (red boxes) and resulting water image of MRSI acquisition (gray shade) overlaid on top of high-resolution MP-RAGE images. (B) Typical region of interest (ROI) analysis is illustrated on the same subjects' MP-RAGE axial image. Number 1 to 18 represent ROIs in the Cerebellar MNI FNIRT Maxprob thr25-2mm SUIT atlas.

Figure 2 (A) Extracted spectra (blue) from nine voxels (2.5 mm x 2.5 mm x 10 mm each) of 5 different volumes of interests with LCModel fit (black). The semi-LASER localization (yellow box) and resulting water image of MRSI acquisition (gray shade) overlaid on top of high-resolution MP-RAGE image. (B) A single spectrum (red box in (A)) illustrates the quality of the achieved spectrum (blue) and LCModel fit (black). Gray box shows residual lipid artifact due to the L2 lipid removal procedure.

Figure 3 Metabolite and CRLB distribution maps after the Gaussian filter obtained with rFOV MRSI from a subject. Normalized metabolite level maps from a nominal voxel dimension of 62.5 μL for tNAA, tCr, tCho, Glx and myo-ins overlaid on an anatomical image. a.u.: arbitrary units

Figure 4 Group-average normalized metabolite maps overlaid on Montreal Neurological Institute-152 template. a.u.: arbitrary units.

Figure 5 Neurochemical profiles from different brain regions determined by LCModel fitting of rFOV MRSI with a nominal resolution of 2.5 mm x 2.5 mm x 10 mm acquired at 3T. Only metabolites and ROIs that were quantified reliably are shown. Metabolites significantly different between regions ($p < 0.05$, ANOVA) were reported in the supporting Information Table S4. Error bars: inter-subject SD (N=5 for all brain regions). a.u.: arbitrary units.

Captions for supporting figures and tables

Figure S1 The MRSI volume of interest positioning for all subjects. The semi-LASER localizations (red boxes) and resulting water image of MRSI acquisitions (gray shade) overlaid on top of high-resolution MP-RAGE image.

Figure S2 Each subject’s MRSI slice and metabolite maps were determined in the MP-RAGE image space using SPM. The Cerebellar MNI FNIRT Maxprob thr25-2mm of the SUIT atlas was transformed to each subject's MPRAGE image space. Mean metabolite levels in cerebellar ROIs were calculated in the center slice of MRSI in the transverse plane. The representative ROI was illustrated for dentate nuclei (white mask in the bottom row).

Table S1 Neurochemical profiles from different brain regions determined by LCModel fitting of rFOV MRSI with a nominal resolution of 2.5 mm x 2.5 mm x 10 mm acquired at 3T. Mean ± standard deviation of normalized metabolite levels is in arbitrary units.

Table S2 Neurochemical profiles from different brain regions determined by LCModel fitting of rFOV MRSI with a nominal resolution of 2.5 mm x 2.5 mm x 10 mm acquired at 3T. Mean ± standard deviation of metabolite ratios (tNAA/tCr, tCho/tCr, Glx/tCr and myo-ins/tCr) is in μmol/g assuming tCr concentration to be 8 μmol/g.

Table S3 Neurochemical profiles from different brain regions determined by LCModel fitting of rFOV MRSI with a nominal resolution of 2.5 mm x 2.5 mm x 10 mm acquired at 3T. Mean ± standard deviation of water scaled metabolite levels is in μmol/g.

Table S4 Pairwise contrasts for normalized metabolite levels with explicit p-values and Benjamini-Hochberg corrected versions of the differences in MRS data across 9 ROIs, resulting in 36 possible pairwise comparisons. We employed a Benjamini-Hochberg correction within each family of comparisons in order to control the false discovery rate of 5 %. Statistically significant P-values are highlighted in bold font.

Table S5 Pairwise contrasts for metabolite ratios (tNAA/tCr, tCho/tCr, Glx/tCr and myo-ins/tCr) with explicit p-values and Benjamini-Hochberg corrected versions of the differences in MRS data across 9 ROIs, resulting in 36 possible pairwise comparisons. We employed a Benjamini-Hochberg correction within each family of comparisons in order to control the false discovery rate of 5 %. Statistically significant P-values are highlighted in bold font.

Table S6 Pairwise contrasts for water scaled metabolite levels with explicit p-values and Benjamini-Hochberg corrected versions of the differences in MRS data across 9 ROIs, resulting in 36 possible pairwise comparisons. We employed a Benjamini-Hochberg correction within each family of comparisons in order to control the false discovery rate of 5 %. Statistically significant P-values are highlighted in bold font.

References

1. Van Essen DC, Donahue CJ, Glasser MF. Development and Evolution of Cerebral and Cerebellar Cortex. Brain Behav Evol 2018;91:158–169 doi: 10.1159/000489943.

2. Howarth C, Gleeson P, Attwell D. Updated energy budgets for neural computation in the neocortex and cerebellum. J Cereb Blood Flow Metab 2012;32:1222–1232 doi: 10.1038/jcbfm.2012.35.

3. Diedrichsen J, Verstynen T, Schlerf J, Wiestler T. Advances in functional imaging of the human cerebellum. Curr. Opin. Neurol. 2010;23:382–387 doi: 10.1097/WCO.0b013e32833be837.

4. Diedrichsen J, Balsters JH, Flavell J, Cussans E, Ramnani N. A probabilistic MR atlas of the human cerebellum. Neuroimage 2009;46:39–46 doi: 10.1016/j.neuroimage.2009.01.045.

5. King M, Hernandez-Castillo CR, Poldrack RA, Ivry RB, Diedrichsen J. Functional boundaries in the human cerebellum revealed by a multi-domain task battery. Nature Neuroscience 2019;22:1371–1378 doi: 10.1038/s41593-019-0436-x.

6. Bürk K. Ataxia Scales for the Clinical Evaluation. In: Gruol DL, Koibuchi N, Manto M, Molinari M, Schmahmann JD, Shen Y, editors. Essentials of Cerebellum and Cerebellar Disorders: A Primer For Graduate Students. Cham: Springer International Publishing; 2016. pp. 513–520. doi: 10.1007/978-3-319-24551-5_69.

7. Fatemi SH. Cerebellar Pathology in Autism. In: Gruol DL, Koibuchi N, Manto M, Molinari M, Schmahmann JD, Shen Y, editors. Essentials of Cerebellum and Cerebellar Disorders: A Primer For Graduate Students. Cham: Springer International Publishing; 2016. pp. 539–543. doi: 10.1007/978-3-319-24551-5_72.

8. Kheradmand A, Kim JS, Zee D. Cerebellum and Oculomotor Deficits. In: Gruol DL, Koibuchi N, Manto M, Molinari M, Schmahmann JD, Shen Y, editors. Essentials of Cerebellum and Cerebellar Disorders: A Primer For Graduate Students. Cham: Springer International Publishing; 2016. pp. 471–475. doi: 10.1007/978-3-319-24551-5_64.

9. Schmahmann JD. The Cerebellar Cognitive Affective Syndrome and the Neuropsychiatry of the Cerebellum. In: Gruol DL, Koibuchi N, Manto M, Molinari M, Schmahmann JD, Shen Y, editors. Essentials of Cerebellum and Cerebellar Disorders: A Primer For Graduate Students. Cham: Springer International Publishing; 2016. pp. 499–511. doi: 10.1007/978-3-319-24551-5_68.

10. Öz G, Alger JR, Barker PB, et al. Clinical proton MR spectroscopy in central nervous system disorders. Radiology 2014;270:658–679.

11. Deelchand DK, Adanyeguh IM, Emir UE, et al. Two-site reproducibility of cerebellar and brainstem neurochemical profiles with short-echo, single-voxel MRS at 3T. Magnetic resonance in medicine 2015;73:1718–1725.

12. Long Z, Dyke JP, Ma R, Huang CC, Louis ED, Dydak U. Reproducibility and effect of tissue composition on cerebellar GABA MRS in an elderly population. NMR Biomed 2015;28:1315–1323 doi: 10.1002/nbm.3381.

13. Maudsley AA, Andronesi OC, Barker PB, et al. Advanced magnetic resonance spectroscopic neuroimaging: Experts' consensus recommendations. NMR in Biomedicine n/a:e4309 doi: 10.1002/nbm.4309.

14. Moser P, Eckstein K, Hingerl L, et al. Intra-session and inter-subject variability of 3D-FID-MRSI using single-echo volumetric EPI navigators at 3T. Magn Reson Med 2020;83:1920–1929 doi: 10.1002/mrm.28076.

15. Lam F, Ma C, Clifford B, Johnson CL, Liang Z-P. High-Resolution 1H-MRSI of the Brain Using SPICE: Data Acquisition and Image Reconstruction. Magn Reson Med 2016;76:1059–1070 doi: 10.1002/mrm.26019.

16. Nassirpour S, Chang P, Henning A. High and ultra-high resolution metabolite mapping of the human brain using 1H FID MRSI at 9.4T. NeuroImage 2016 doi: 10.1016/j.neuroimage.2016.12.065.

17. Hingerl L, Strasser B, Moser P, et al. Clinical High-Resolution 3D-MR Spectroscopic Imaging of the Human Brain at 7 T. Investigative Radiology 2020;55:239–248 doi: 10.1097/RLI.0000000000000626.

18. Maudsley AA, Domenig C, Govind V, et al. Mapping of Brain Metabolite Distributions by Volumetric Proton MR Spectroscopic Imaging (MRSI). Magn Reson Med 2009;61:548–559 doi: 10.1002/mrm.21875.

19. Jacobs MA, Horská A, van Zijl PC, Barker PB. Quantitative proton MR spectroscopic imaging of normal human cerebellum and brain stem. Magn Reson Med 2001;46:699–705.

20. Pfeuffer J, van de Moortele P-F, Yacoub E, et al. Zoomed Functional Imaging in the Human Brain at 7 Tesla with Simultaneous High Spatial and High Temporal Resolution. NeuroImage 2002;17:272–286 doi: 10.1006/nimg.2002.1103.

21. SUN H, FESSLER JA, NOLL DC, NIELSEN J-F. Rapid inner-volume imaging in the steady-state with 3D selective excitation and small-tip fast recovery (STFR) imaging. Magn Reson Med 2016;76:1217–1223 doi: 10.1002/mrm.26026.

22. Golay X, Gillen J, van Zijl PCM, Barker PB. Scan time reduction in proton magnetic resonance spectroscopic imaging of the human brain. Magn Reson Med 2002;47:384–387 doi: 10.1002/mrm.10038.

23. Maudsley AA, Matson GB, Hugg JW, Weiner MW. Reduced phase encoding in spectroscopic imaging. Magnetic Resonance in Medicine 1994;31:645–651 doi: 10.1002/mrm.1910310610.

24. Chiew M, Jiang W, Burns B, et al. Density-weighted concentric rings k-space trajectory for 1H magnetic resonance spectroscopic imaging at 7 T. NMR Biomed 2018;31 doi: 10.1002/nbm.3838.

25. Emir UE, Burns B, Chiew M, Jezzard P, Thomas MA. Non-water-suppressed short-echo-time magnetic resonance spectroscopic imaging using a concentric ring k-space trajectory. NMR Biomed 2017;30 doi: 10.1002/nbm.3714.

26. Steel A, Chiew M, Jezzard P, et al. Metabolite-cycled density-weighted concentric rings k-space trajectory (DW-CRT) enables high-resolution 1 H magnetic resonance spectroscopic imaging at 3-Tesla. Scientific Reports 2018;8:7792 doi: 10.1038/s41598-018-26096-y.

27. Fessler JA, Sutton BP. Nonuniform fast Fourier transforms using min-max interpolation. IEEE Transactions on Signal Processing 2003;51:560–574 doi: 10.1109/TSP.2002.807005.

28. Cabanes E, Confort-Gouny S, Le Fur Y, Simond G, Cozzone PJ. Optimization of residual water signal removal by HLSVD on simulated short echo time proton MR spectra of the human brain. J. Magn. Reson. 2001;150:116–125 doi: 10.1006/jmre.2001.2318.

29. Bilgic B, Chatnuntawech I, Fan AP, et al. Fast image reconstruction with L2-regularization. J Magn Reson Imaging 2014;40:181–191 doi: 10.1002/jmri.24365.

30. Provencher SW. Automatic quantitation of localized in vivo 1H spectra with LCModel. NMR Biomed 2001;14:260–264.

31. Quadrelli S, Mountford C, Ramadan S. Hitchhiker's Guide to Voxel Segmentation for Partial Volume Correction of In Vivo Magnetic Resonance Spectroscopy. Magn Reson Insights 2016;9:1–8 doi: 10.4137/MRI.S32903.

32. Jenkinson M, Beckmann CF, Behrens TEJ, Woolrich MW, Smith SM. FSL. NeuroImage 2012;62:782–790 doi: 10.1016/j.neuroimage.2011.09.015.

33. Benjamini Y, Hochberg Y. Controlling the False Discovery Rate: A Practical and Powerful Approach to Multiple Testing. Journal of the Royal Statistical Society. Series B (Methodological) 1995;57:289–300.

34. Alhulail AA, Patterson DA, Xia P, et al. Fat–water separation by fast metabolite cycling magnetic resonance spectroscopic imaging at 3 T: A method to generate separate quantitative distribution maps of musculoskeletal lipid components. Magnetic Resonance in Medicine n/a doi: 10.1002/mrm.28228.

35. Keil B, Blau JN, Biber S, et al. A 64-channel 3T array coil for accelerated brain MRI. Magn Reson Med 2013;70:248–258 doi: 10.1002/mrm.24427.

36. Hangel G, Strasser B, Považan M, et al. Ultra-high resolution brain metabolite mapping at 7 T by short-TR Hadamard-encoded FID-MRSI. Neuroimage 2018;168:199–210 doi: 10.1016/j.neuroimage.2016.10.043.

37. Klauser A, Courvoisier S, Kasten J, et al. Fast high-resolution brain metabolite mapping on a clinical 3T MRI by accelerated
1 H-FID-MRSI and low-rank constrained
reconstruction. Magn Reson Med 2019;81:2841–2857 doi: 10.1002/mrm.27623.

38. Emir UE, Auerbach EJ, Moortele P-FVD, et al. Regional neurochemical profiles in the human brain measured by 1H MRS at 7 T using local B1 shimming. NMR in Biomedicine 2012;25:152–160.

39. Jaeger D, Lu H. Cerebellar Nuclei. In: Gruol DL, Koibuchi N, Manto M, Molinari M, Schmahmann JD, Shen Y, editors. Essentials of Cerebellum and Cerebellar Disorders: A Primer For Graduate Students. Cham: Springer International Publishing; 2016. pp. 311–315. doi: 10.1007/978-3-319-24551-5_42.

40. Moffett JR, Namboodiri AMA. Expression of N-Acetylaspartate and N-Acetylaspartylglutamate in the Nervous System. In: Moffett JR, Tieman SB, Weinberger DR, Coyle JT, Namboodiri AMA, editors. N-Acetylaspartate. Advances in Experimental Medicine and Biology. Boston, MA: Springer US; 2006. pp. 7–26. doi: 10.1007/0-387-30172-0_2.

41. Fa A, Lr C, Lt G, et al. Equal Numbers of Neuronal and Nonneuronal Cells Make the Human Brain an Isometrically Scaled-Up Primate Brain. The Journal of comparative neurology. https://pubmed.ncbi.nlm.nih.gov/19226510/?dopt=Abstract. Published April 10, 2009. Accessed May 19, 2020 doi: 10.1002/cne.21974.

42. Palomero-Gallagher N, Zilles K. Chapter 24 - Cyto- and receptor architectonic mapping of the human brain. In: Huitinga I, Webster MJ, editors. Handbook of Clinical Neurology. Vol. 150. Brain Banking. Elsevier; 2018. pp. 355–387. doi: 10.1016/B978-0-444-63639-3.00024-4.

43. Shilling RZ, Robbie TQ, Bailloeul T, Mewes K, Mersereau RM, Brummer ME. A Super-Resolution Framework for 3-D High-Resolution and High-Contrast Imaging Using 2-D Multislice MRI. IEEE Transactions on Medical Imaging 2009;28:633–644 doi: 10.1109/TMI.2008.2007348.

44. Tannús A, Garwood M. Adiabatic pulses. NMR Biomed 1997;10:423–434.

45. Dydak U, Meier D, Lamerichs R, Boesiger P. Trading Spectral Separation at 3T for Acquisition Speed in Multi Spin-Echo Spectroscopic Imaging. American Journal of Neuroradiology 2006;27:1441–1446.

46. Chang P, Nassirpour S, Avdievitch N, Henning A. Non-water-suppressed 1 H FID-MRSI at 3T and 9.4T. Magn Reson Med 2018;80:442–451 doi: 10.1002/mrm.27049.

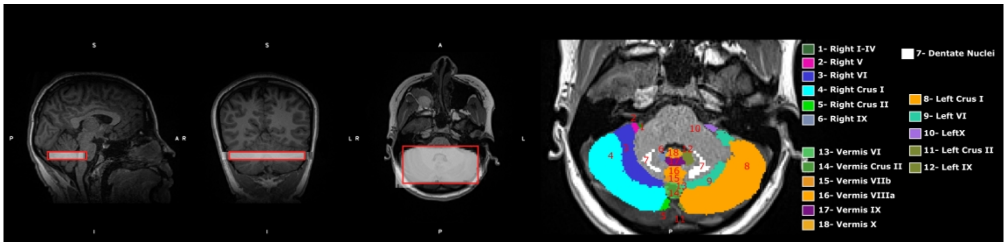

Representative semi-LASER localization (red boxes) and resulting water image of MRSI acquisition (gray shade) overlaid on top of high-resolution MP-RAGE images. (B) Typical region of interest (ROI) analysis is illustrated on the same subjects' MP-RAGE axial image. Number 1 to 18 represent ROIs in the Cerebellar MNI FNIRT Maxprob thr25-2mm SUIT atlas.

702x167mm (300 x 300 DPI)

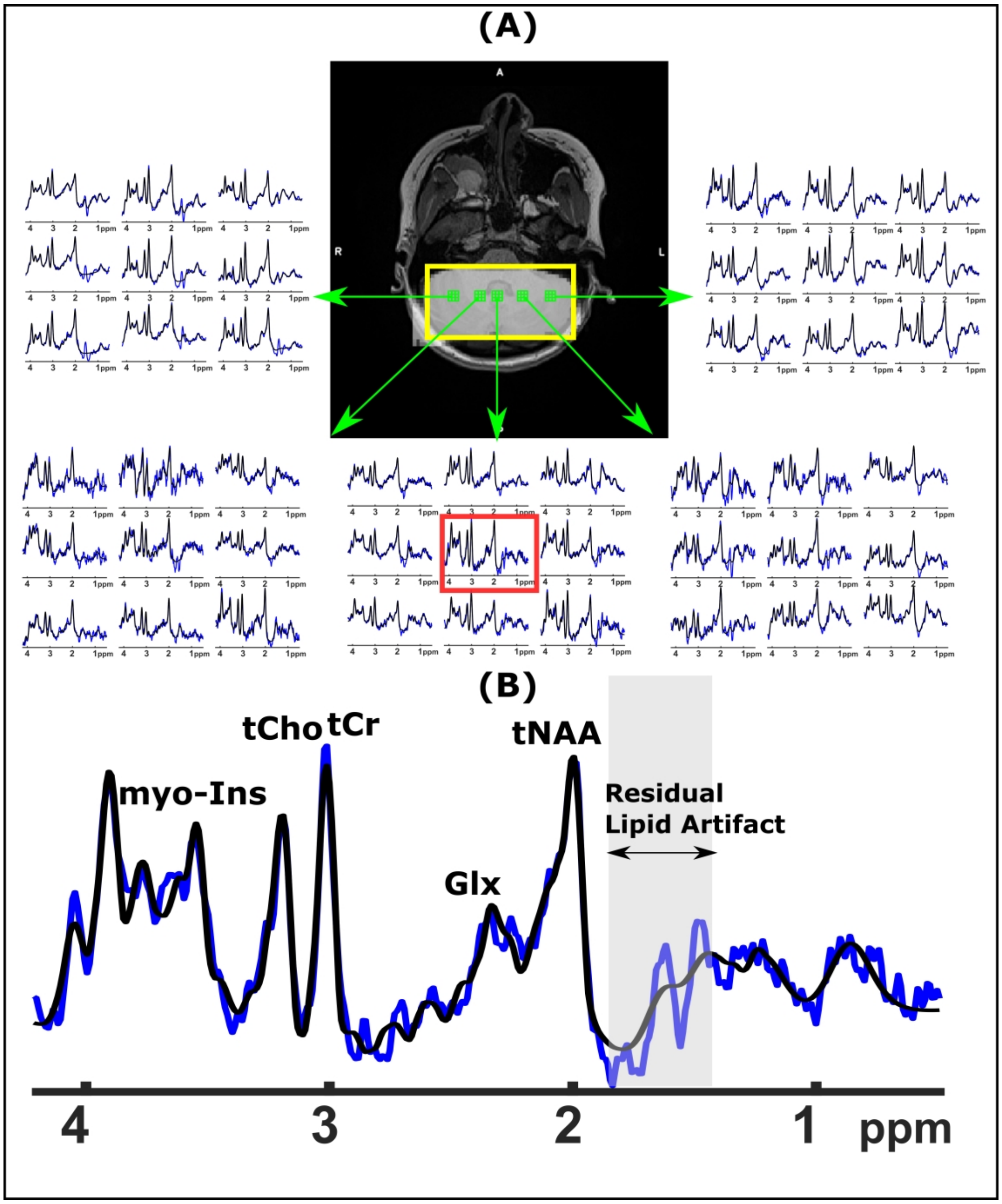

Figure 2 (A) Extracted spectra (blue) from nine voxels (2.5 mm x 2.5 mm x 10 mm each) of 5 different volumes of interests with LCModel fit (black). The semi-LASER localization (yellow box) and resulting water image of MRSI acquisition (gray shade) overlaid on top of high-resolution MP-RAGE image. (B) A single spectrum (red box in (A)) illustrates the quality of the achieved spectrum (blue) and LCModel fit (black). Gray box shows residual lipid artifact due to the L2 lipid removal procedure.

422x508mm (300 x 300 DPI)

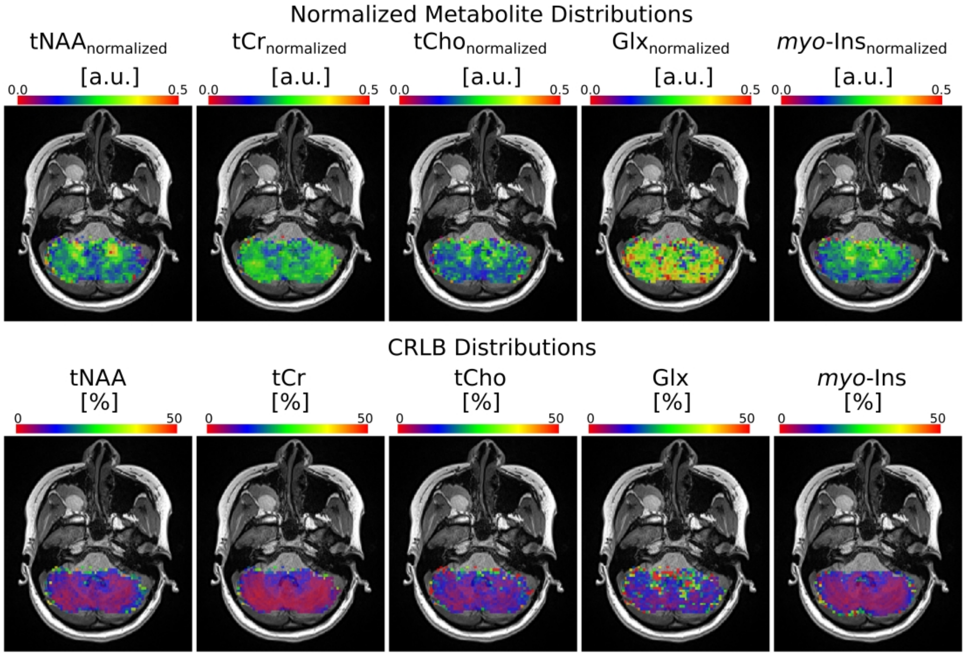

Figure 3 Metabolite and CRLB distribution maps after the Gaussian filter obtained with rFOV MRSI from a subject. Normalized metabolite level maps from a nominal voxel dimension of 62.5 ☐L for tNAA, tCr, tCho, Glx and myo-ins overlaid on an anatomical image. a.u.: arbitrary units

502x336mm (300 x 300 DPI)

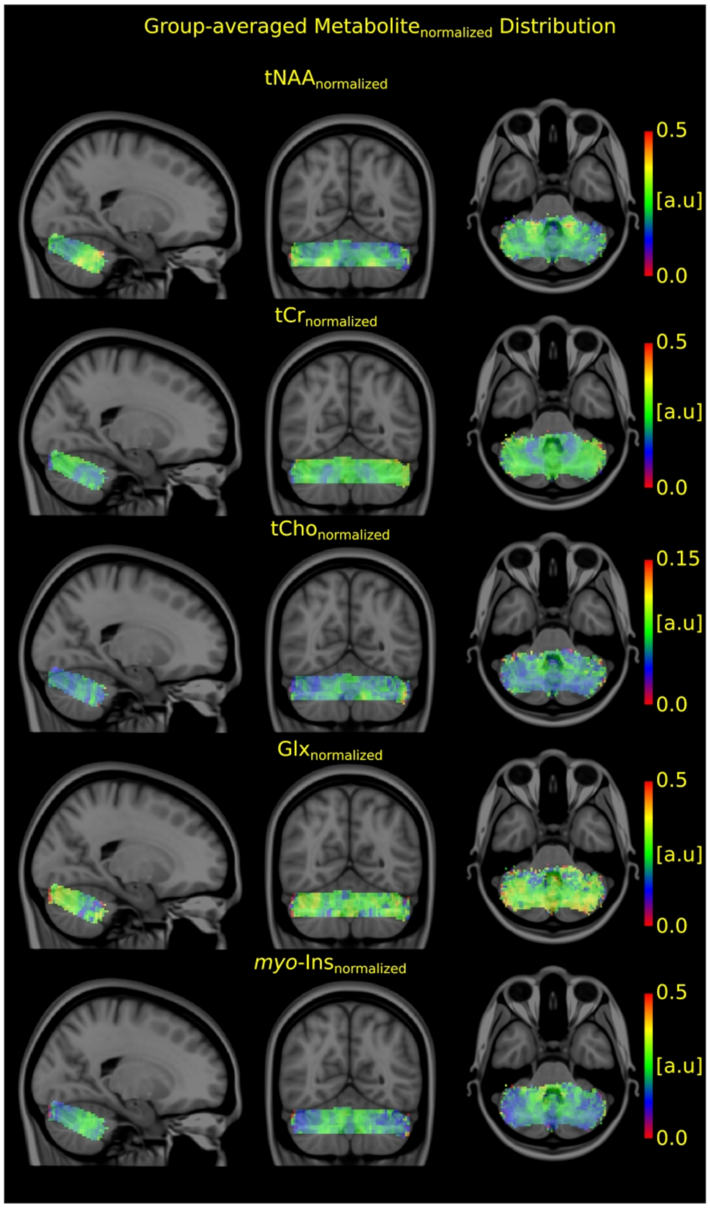

Figure 4 Group-average normalized metabolite maps overlaid on Montreal Neurological Institute-152 template. a.u.: arbitrary units.

199x340mm (300 x 300 DPI)

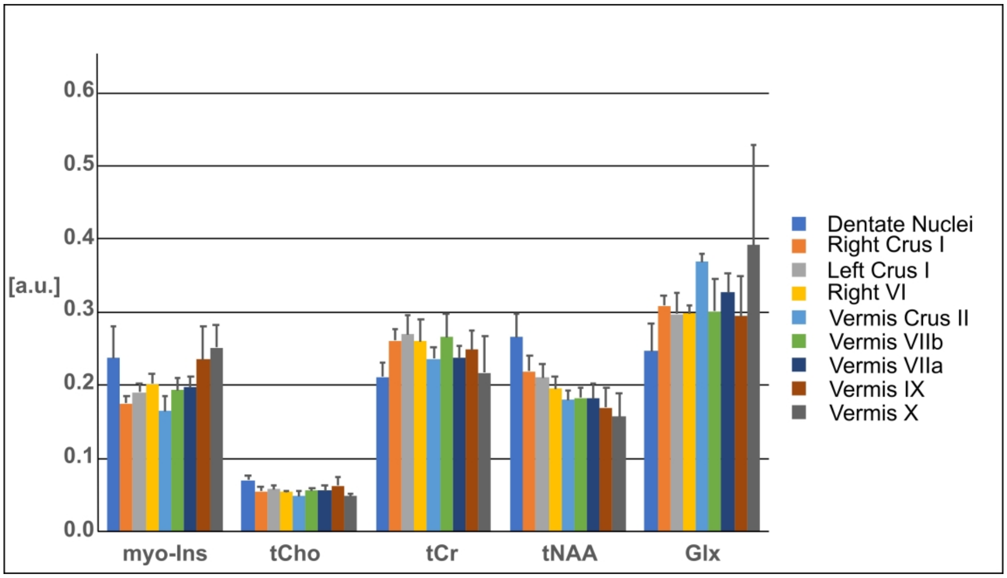

Figure 5 Neurochemical profiles from different brain regions determined by LCModel fitting of rFOV MRSI with a nominal resolution of 2.5 mm x 2.5 mm x 10 mm acquired at 3T. Only metabolites and ROIs that were quantified reliably are shown. Metabolites significantly different between regions ($p < 0.05$, ANOVA) were reported in the supporting Information Table S2. Error bars: inter-subject SD (N=5 for all brain regions). a.u.: arbitrary units.

252x144mm (300 x 300 DPI)

`Supporting Information

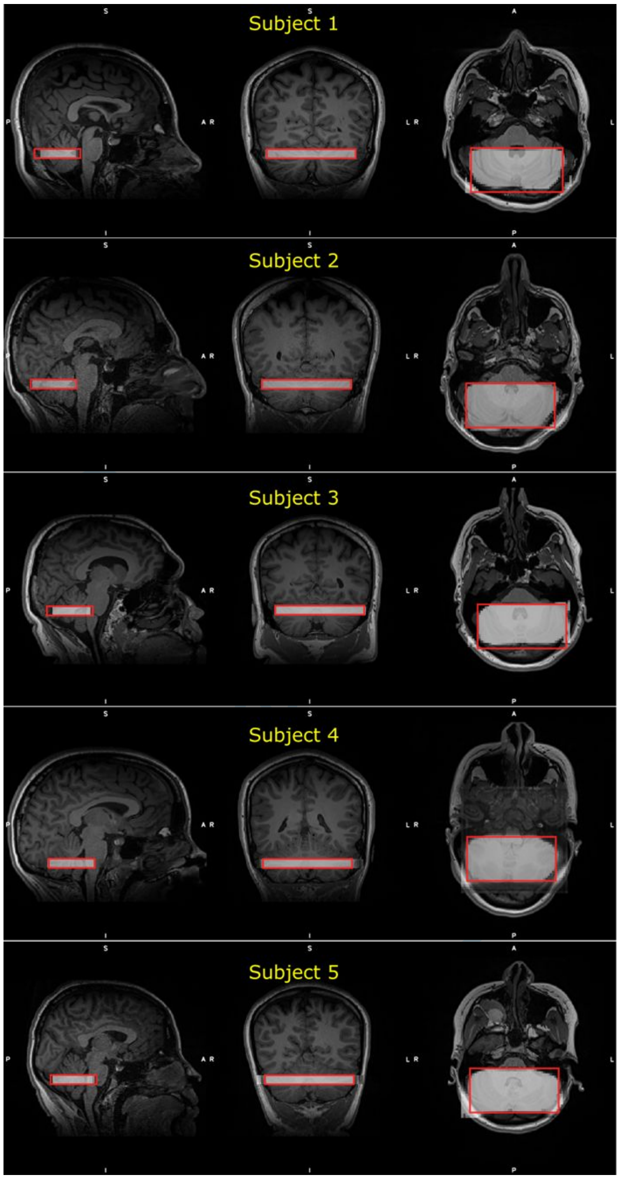

Figure S1 The MRSI volume of interest positioning for all subjects. The semi-LASER localizations (red boxes) and resulting water image of MRSI acquisitions (gray shade) overlaid on top of high-resolution MP-RAGE image.

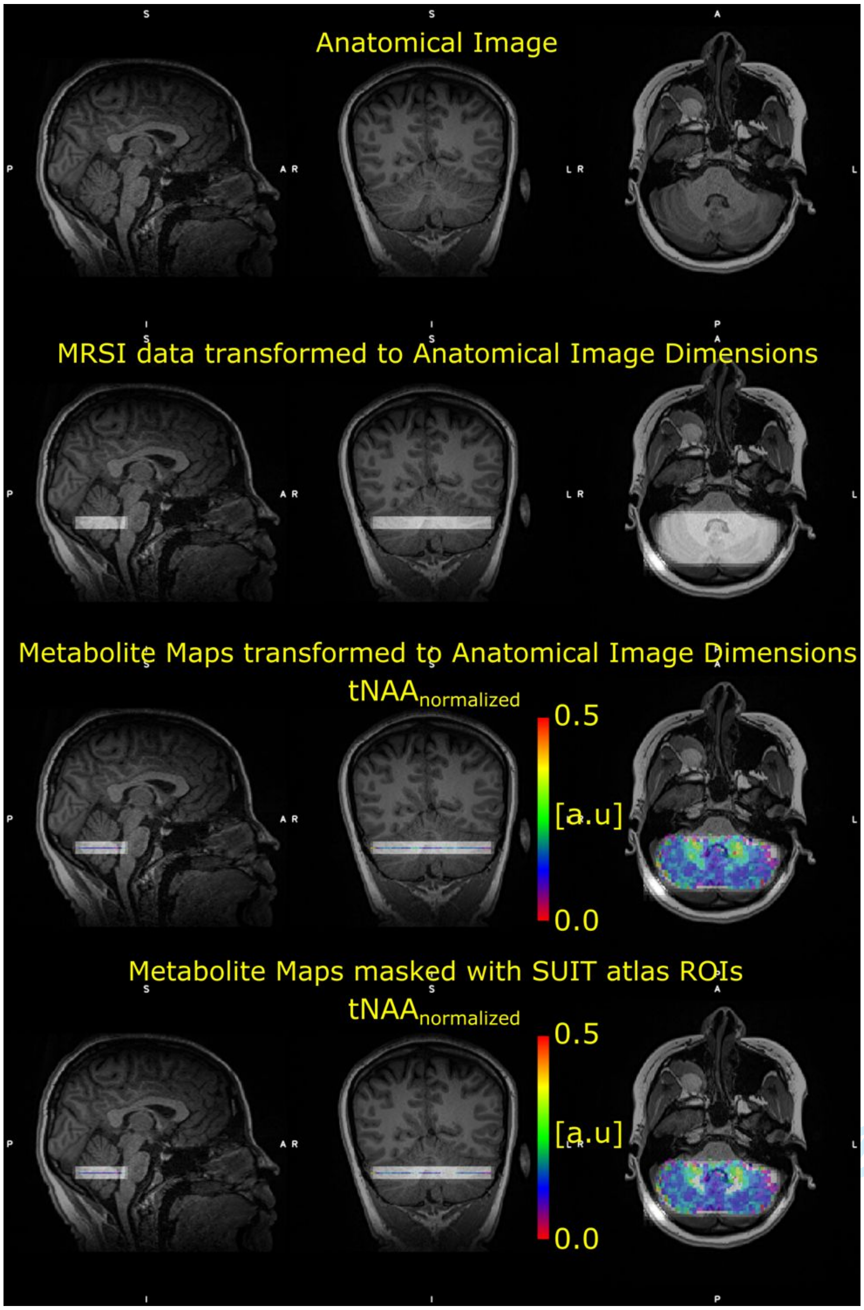

Figure S2 Each subject’s MRSI slice and metabolite maps were determined in the MP-RAGE image space using SPM. The Cerebellar MNI FNIRT Maxprob thr25-2mm of the SUIT atlas was transformed to each subject's MPRAGE image space. Mean metabolite levels in cerebellar ROIs were calculated in the center slice of MRSI in the transverse plane. The representative ROI was illustrated for dentate nuclei (white mask in the bottom row).

Table S1 Neurochemical profiles from different brain regions determined by LCModel fitting of rFOV MRSI with a nominal resolution of 2.5 mm x 2.5 mm x 10 mm acquired at 3T. Mean ± standard deviation of normalized metabolite levels is in arbitrary units.

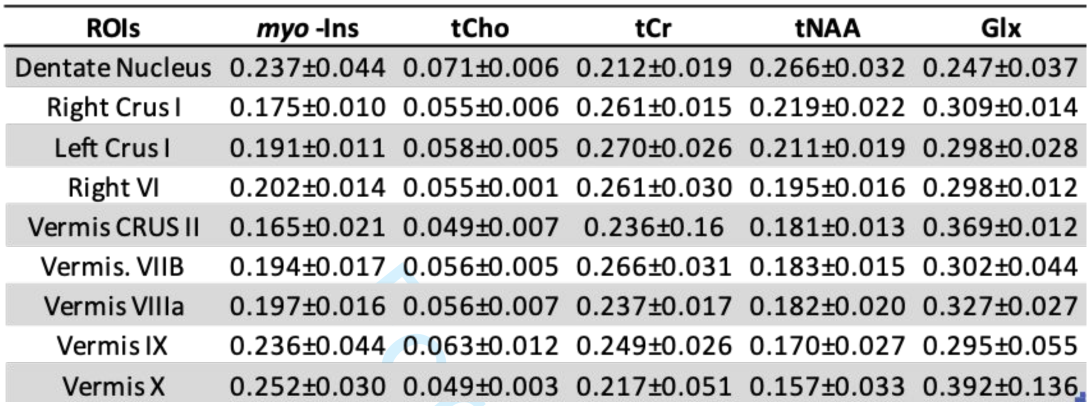

ROIs	*myo* -Ins	tCho	tCr	tNAA	Glx
Dentate Nucleus	0.237±0.044	0.071±0.006	0.212±0.019	0.266±0.032	0.247±0.037
Right Crus I	0.175±0.010	0.055±0.006	0.261±0.015	0.219±0.022	0.309±0.014
Left Crus I	0.191±0.011	0.058±0.005	0.270±0.026	0.211±0.019	0.298±0.028
Right VI	0.202±0.014	0.055±0.001	0.261±0.030	0.195±0.016	0.298±0.012
Vermis CRUS II	0.165±0.021	0.049±0.007	0.236±0.16	0.181±0.013	0.369±0.012
Vermis. VIIB	0.194±0.017	0.056±0.005	0.266±0.031	0.183±0.015	0.302±0.044
Vermis VIIIa	0.197±0.016	0.056±0.007	0.237±0.017	0.182±0.020	0.327±0.027
Vermis IX	0.236±0.044	0.063±0.012	0.249±0.026	0.170±0.027	0.295±0.055
Vermis X	0.252±0.030	0.049±0.003	0.217±0.051	0.157±0.033	0.392±0.136

Table S2 Neurochemical profiles from different brain regions determined by LCModel fitting of rFOV MRSI with a nominal resolution of 2.5 mm x 2.5 mm x 10 mm acquired at 3T. Mean ± standard deviation of metabolite ratios (tNAA/tCr, tCho/tCr, Glx/tCr and myo-ins/tCr) is in μmol/g assuming tCr concentration to be 8 μmol/g.

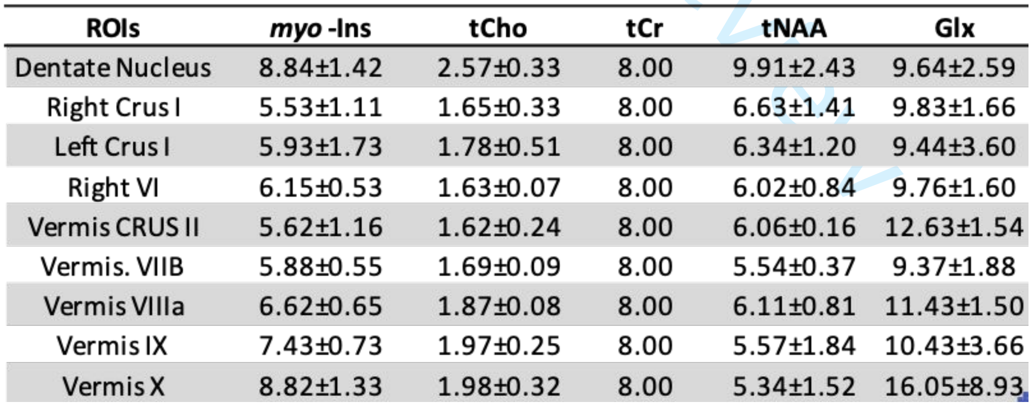

ROIs	*myo* -Ins	tCho	tCr	tNAA	Glx
Dentate Nucleus	8.84±1.42	2.57±0.33	8.00	9.91±2.43	9.64±2.59
Right Crus I	5.53±1.11	1.65±0.33	8.00	6.63±1.41	9.83±1.66
Left Crus I	5.93±1.73	1.78±0.51	8.00	6.34±1.20	9.44±3.60
Right VI	6.15±0.53	1.63±0.07	8.00	6.02±0.84	9.76±1.60
Vermis CRUS II	5.62±1.16	1.62±0.24	8.00	6.06±0.16	12.63±1.54
Vermis. VIIB	5.88±0.55	1.69±0.09	8.00	5.54±0.37	9.37±1.88
Vermis VIIIa	6.62±0.65	1.87±0.08	8.00	6.11±0.81	11.43±1.50
Vermis IX	7.43±0.73	1.97±0.25	8.00	5.57±1.84	10.43±3.66
Vermis X	8.82±1.33	1.98±0.32	8.00	5.34±1.52	16.05±8.93

Table S3 Neurochemical profiles from different brain regions determined by LCModel fitting of rFOV MRSI with a nominal resolution of 2.5 mm x 2.5 mm x 10 mm acquired at 3T. Mean ± standard deviation of water scaled metabolite levels is in μmol/g.

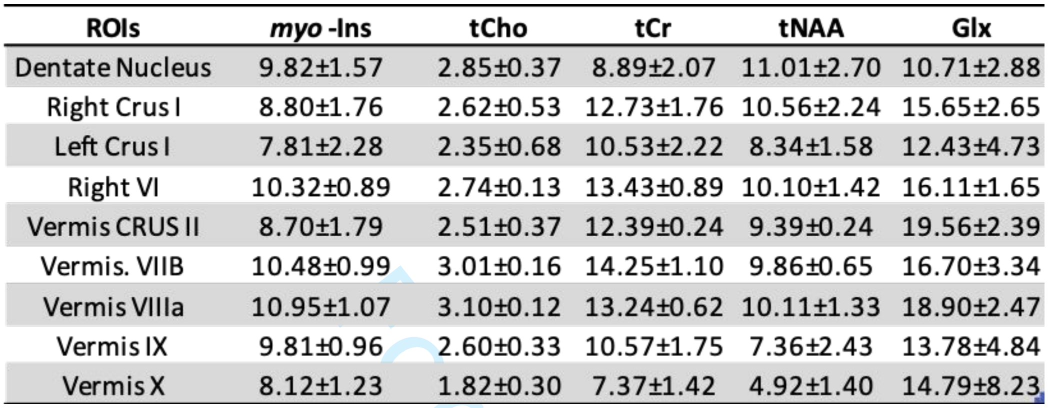

ROIs	*myo* -Ins	tCho	tCr	tNAA	Glx
Dentate Nucleus	9.82±1.57	2.85±0.37	8.89±2.07	11.01±2.70	10.71±2.88
Right Crus I	8.80±1.76	2.62±0.53	12.73±1.76	10.56±2.24	15.65±2.65
Left Crus I	7.81±2.28	2.35±0.68	10.53±2.22	8.34±1.58	12.43±4.73
Right VI	10.32±0.89	2.74±0.13	13.43±0.89	10.10±1.42	16.11±1.65
Vermis CRUS II	8.70±1.79	2.51±0.37	12.39±0.24	9.39±0.24	19.56±2.39
Vermis. VIIB	10.48±0.99	3.01±0.16	14.25±1.10	9.86±0.65	16.70±3.34
Vermis VIIIa	10.95±1.07	3.10±0.12	13.24±0.62	10.11±1.33	18.90±2.47
Vermis IX	9.81±0.96	2.60±0.33	10.57±1.75	7.36±2.43	13.78±4.84
Vermis X	8.12±1.23	1.82±0.30	7.37±1.42	4.92±1.40	14.79±8.23

Table S4 Pairwise contrasts for normalized metabolite levels with explicit p-values and Benjamini-Hochberg corrected versions of the differences in MRS data across 9 ROIs, resulting in 36 possible pairwise comparisons. We employed a Benjamini-Hochberg correction within each family of comparisons in order to control the false discovery rate of 5 %. Statistically significant P-values are highlighted in bold font.

Statistical Test										
	tNAA		tCr		tCho		Glx		myo-Ins	
Region vs Region	Probt	B-H cutoff	Probt	B-H cutoff	Probt	B-H cutoff	Probt	B-H cutoff	Probt	B-H cutoff
Dendate vs. LeftCrusI	**0.0010**	**0.0111**	**0.0007**	**0.0014**	**0.005**	**0.010**	0.1548	0.0222	**0.0095**	**0.0111**
Dendate vs. RightCrusI	**0.0043**	**0.0153**	**0.0027**	**0.0056**	**0.001**	**0.004**	0.0855	0.0153	**0.0009**	**0.0042**
Dendate vs. RightVI	**0.0001**	**0.0083**	**0.0065**	**0.0069**	**0.002**	**0.006**	0.1739	0.0236	0.0544	0.0208
Dendate vs. VERMISCRUSII	**Probt<<0.0001**	**0.0042**	0.1039	0.0167	**Probt<<0.0001**	**0.003**	0.0048	0.0028	**0.0012**	**0.0069**
Dendate vs. VermisIX	**Probt<<0.0001**	**0.0028**	0.0202	0.0125	0.077	0.018	0.1775	0.0250	0.9451	0.0500
Dendate vs. VERMISVIIB	**0.0001**	**0.0069**	**0.0025**	**0.0042**	**0.005**	**0.008**	0.1829	0.0264	0.0426	0.0181
Dendate vs. VermisVIIIa	**Probt<<0.0001**	**0.0056**	0.0939	0.0153	**0.006**	**0.013**	0.0555	0.0111	0.0618	0.0222
Dendate vs. VermisX	**Probt<<0.0001**	**0.0014**	0.8014	0.0458	**Probt<<0.0001**	**0.001**	**0.0005**	**0.0014**	0.4294	0.0389
LeftCrusI vs. RightCrusI	0.5759	0.0458	0.5900	0.0403	0.490	0.036	0.7511	0.0389	0.3700	0.0361
LeftCrusI vs. RightVI	0.3536	0.0347	0.5194	0.0361	0.524	0.038	0.9869	0.0500	0.5486	0.0403
LeftCrusI vs. VERMISCRUSII	0.0973	0.0236	0.1227	0.0181	0.063	0.015	0.0837	0.0139	0.2314	0.0333
LeftCrusI vs. VermisIX	**0.0117**	**0.0167**	0.1819	0.0264	0.231	0.035	0.9377	0.0486	**0.0113**	**0.0139**
LeftCrusI vs. VERMISVIIB	0.1225	0.0278	0.9557	0.0486	0.677	0.039	0.9215	0.0444	0.7919	0.0458
LeftCrusI vs. VermisVIIIa	0.1102	0.0250	0.1351	0.0194	0.747	0.040	0.4702	0.0306	0.6592	0.0417
LeftCrusI vs. VermisX	**0.0024**	**0.0125**	0.0024	0.0028	0.054	0.014	0.0157	0.0056	**0.0020**	**0.0097**
RightCrusI vs. RightVI	0.1509	0.0292	0.8885	0.0472	0.989	0.050	0.7774	0.0403	0.1545	0.0292
RightCrusI vs. VERMISCRUSII	0.0358	0.0194	0.2697	0.0292	0.195	0.031	0.1407	0.0194	0.6630	0.0431
RightCrusI vs. VermisIX	**0.0029**	**0.0139**	0.4171	0.0347	0.065	0.017	0.6928	0.0375	**0.0011**	**0.0056**
RightCrusI vs. VERMISVIIB	0.0465	0.0222	0.6061	0.0417	0.854	0.044	0.8600	0.0417	0.3030	0.0347
RightCrusI vs. VermisVIIIa	0.0412	0.0208	0.2924	0.0306	0.781	0.042	0.6529	0.0361	0.2294	0.0319
RightCrusI vs. VermisX	**0.0006**	**0.0097**	**0.0086**	**0.0097**	0.187	0.029	0.0310	0.0083	**0.0002**	**0.0014**
RightVI vs. VERMISCRUSII	0.4237	0.0361	0.3535	0.0319	0.210	0.033	0.1001	0.0167	0.1019	0.0264
RightVI vs. VermisIX	0.1214	0.0264	0.5334	0.0375	0.083	0.019	0.9282	0.0458	0.0622	0.0236
RightVI vs. VERMISVIIB	0.4932	0.0417	0.5432	0.0389	0.870	0.046	0.9364	0.0472	0.7856	0.0444
RightVI vs. VermisVIIIa	0.4603	0.0389	0.3792	0.0333	0.800	0.043	0.4987	0.0319	0.9178	0.0486
RightVI vs. VermisX	0.0311	0.0181	0.0160	0.0111	0.205	0.032	0.0220	0.0069	**0.0124**	**0.0153**
VERMISCRUSII vs. VermisIX	0.5417	0.0444	0.6758	0.0431	**0.006**	**0.011**	0.0731	0.0125	**0.0014**	**0.0083**
VERMISCRUSII vs. VERMISVIIB	0.9131	0.0472	0.1462	0.0208	0.187	0.028	0.1409	0.0208	0.1901	0.0306
VERMISCRUSII vs. VermisVIIIa	0.9533	0.0486	0.9620	0.0500	0.161	0.024	0.3504	0.0278	0.1437	0.0278
VERMISCRUSII vs. VermisX	0.2081	0.0333	0.1810	0.0250	0.935	0.049	0.5902	0.0347	**0.0003**	**0.0028**
VermisIX vs. VermisVIIIa	0.4997	0.0431	0.7144	0.0444	0.177	0.025	0.4303	0.0292	0.0697	0.0250
VermisIX vs. VermisX	0.4332	0.0375	0.0493	0.0139	**0.004**	**0.007**	0.0132	0.0042	0.3932	0.0375
VERMISVIIB vs. VermisIX	0.4650	0.0403	0.2308	0.0278	0.150	0.021	0.8680	0.0431	0.0483	0.0194
VERMISVIIB vs. VermisVIIIa	0.9597	0.0500	0.1592	0.0222	0.933	0.047	0.5761	0.0333	0.8727	0.0472
VERMISVIIB vs. VermisX	0.1707	0.0306	**0.0067**	**0.0083**	0.183	0.026	0.0391	0.0097	**0.0112**	**0.0125**
VermisVIIIa vs. VermisX	0.1873	0.0319	0.1661	0.0236	0.156	0.022	0.1300	0.0181	0.0167	0.0167

Table S5 Pairwise contrasts for metabolite ratios (tNAA/tCr, tCho/tCr, Glx/tCr and myo-ins/tCr) with explicit p-values and Benjamini-Hochberg corrected versions of the differences in MRS data across 9 ROIs, resulting in 36 possible pairwise comparisons. We employed a Benjamini-Hochberg correction within each family of comparisons in order to control the false discovery rate of 5 %. Statistically significant P-values are highlighted in bold font.

Statistical Test	tNAA		tCr		tCho		Glx		myo-Ins	
Region vs Region	Probt	B-H cutoff	Probt	B-H cutoff	Probt	B-H cutoff	Probt	B-H cutoff	Probt	B-H cutoff
Dendate vs. LeftCrusI	**0.0042**	**0.0083**	NA	NA	**Probt<<0.0001**	**0.0028**	0.8897	0.0347	**0.0001**	**0.0097**
Dendate vs. RightCrusI	0.0101	0.0097	NA	NA	**Probt<<0.0001**	**0.0014**	0.9716	0.0458	**Probt<<0.0001**	**0.0042**
Dendate vs. RightVI	**0.0021**	**0.0042**	NA	NA	**0.0001**	**0.0042**	0.8751	0.0319	**0.0007**	**0.0153**
Dendate vs. VERMISCRUSII	**0.0035**	**0.0056**	NA	NA	**0.0001**	**0.0056**	0.7064	0.0194	**0.0001**	**0.0111**
Dendate vs. VermisIX	**0.0003**	**0.0014**	NA	NA	**0.0017**	**0.0097**	0.9613	0.0444	0.023	0.0222
Dendate vs. VERMISVIIB	**0.0012**	**0.0028**	NA	NA	**0.0001**	**0.0069**	0.8579	0.0292	**0.0003**	**0.0125**
Dendate vs. VermisVIIIa	**0.0041**	**0.0069**	NA	NA	**0.0015**	**0.0083**	0.8708	0.0306	**0.0045**	**0.0181**
Dendate vs. VermisX	0.0132	0.0111	NA	NA	**0.0083**	**0.0111**	0.0178	0.0069	0.2348	0.0306
LeftCrusI vs. RightCrusI	0.7251	0.0417	NA	NA	0.979	0.0486	0.9179	0.0403	0.5588	0.0417
LeftCrusI vs. RightVI	0.6531	0.0333	NA	NA	0.9959	0.05	0.9789	0.0486	0.5538	0.0403
LeftCrusI vs. VERMISCRUSII	0.6296	0.0292	NA	NA	0.7252	0.0375	0.6198	0.0153	0.6334	0.0431
LeftCrusI vs. VermisIX	0.3332	0.0181	NA	NA	0.171	0.0236	0.9281	0.0417	0.0296	0.0236
LeftCrusI vs. VERMISVIIB	0.3746	0.0194	NA	NA	0.8382	0.0417	0.9529	0.0431	0.8917	0.0486
LeftCrusI vs. VermisVIIIa	0.6689	0.0347	NA	NA	0.509	0.0319	0.7775	0.0236	0.3709	0.0375
LeftCrusI vs. VermisX	0.7741	0.0431	NA	NA	0.0936	0.0153	0.0131	0.0014	**Probt<<0.0001**	**0.0028**
RightCrusI vs. RightVI	0.4366	0.0222	NA	NA	0.9762	0.0472	0.9015	0.0375	0.2585	0.0319
RightCrusI vs. VERMISCRUSII	0.4332	0.0208	NA	NA	0.7422	0.0403	0.6837	0.0181	0.9828	0.05
RightCrusI vs. VermisIX	0.1911	0.0125	NA	NA	0.1633	0.0208	0.9897	0.05	**0.0075**	**0.0194**
RightCrusI vs. VERMISVIIB	0.2364	0.0153	NA	NA	0.8558	0.0444	0.8821	0.0333	0.7167	0.0444
RightCrusI vs. VermisVIIIa	0.4656	0.0236	NA	NA	0.4948	0.0306	0.8467	0.0264	0.1685	0.0278
RightCrusI vs. VermisX	0.9644	0.0486	NA	NA	0.0892	0.0139	0.0165	0.0042	**Probt<<0.0001**	**0.0014**
RightVI vs. VERMISCRUSII	0.9469	0.0444	NA	NA	0.7347	0.0389	0.6187	0.0125	0.3402	0.0347
RightVI vs. VermisIX	0.6392	0.0306	NA	NA	0.199	0.025	0.9112	0.0389	0.133	0.0264
RightVI vs. VERMISVIIB	0.6464	0.0319	NA	NA	0.8424	0.0431	0.9736	0.0472	0.5244	0.0389
RightVI vs. VermisVIIIa	0.9888	0.05	NA	NA	0.5328	0.0333	0.7692	0.0222	0.7333	0.0458
RightVI vs. VermisX	0.486	0.0264	NA	NA	0.1107	0.0181	0.017	0.0056	**Probt<<0.0001**	**0.0083**
VERMISCRUSII vs. VermisIX	0.7178	0.0403	NA	NA	0.1293	0.0194	0.6756	0.0167	0.0215	0.0208
VERMISCRUSII vs. VERMISVIIB	0.7135	0.0389	NA	NA	0.8942	0.0458	0.6196	0.0139	0.7562	0.0472
VERMISCRUSII vs. VermisVIIIa	0.9608	0.0458	NA	NA	0.3641	0.0264	0.8479	0.0278	0.2161	0.0292
VERMISCRUSII vs. VermisX	0.477	0.025	NA	NA	0.0752	0.0125	0.0753	0.0111	**Probt<<0.0001**	**0.0056**
VermisIX vs. VermisVIIIa	0.6773	0.0361	NA	NA	0.594	0.0347	0.8379	0.025	0.3059	0.0333
VermisIX vs. VermisX	0.2333	0.0139	NA	NA	0.6811	0.0361	0.016	0.0028	**0.0017**	**0.0167**
VERMISVIIB vs. VermisIX	0.9608	0.0472	NA	NA	0.1683	0.0222	0.891	0.0361	0.0458	0.025
VERMISVIIB vs. VermisVIIIa	0.6773	0.0375	NA	NA	0.4371	0.0292	0.7601	0.0208	0.3493	0.0361
VERMISVIIB vs. VermisX	0.2733	0.0167	NA	NA	0.099	0.0167	0.0241	0.0083	**Probt<<0.0001**	**0.0069**
VermisVIIIa vs. VermisX	0.5097	0.0278	NA	NA	0.3895	0.0278	0.0494	0.0097	**0.0005**	**0.0139**

Table S6 Pairwise contrasts for water scaled metabolite levels with explicit p-values and Benjamini-Hochberg corrected versions of the differences in MRS data across 9 ROIs, resulting in 36 possible pairwise comparisons. We employed a Benjamini-Hochberg correction within each family of comparisons in order to control the false discovery rate of 5 %. Statistically significant P-values are highlighted in bold font.

Statistical Test	tNAA		tCr		tCho		Glx		myo-Ins	
Region vs Region	Probt	B-H cutoff	Probt	B-H cutoff	Probt	B-H cutoff	Probt	B-H cutoff	Probt	B-H cutoff
Dendate vs. LeftCrusI	**0.0026**	**0.0139**	0.0393	0.0306	0.0225	0.0111	0.5179	0.0361	0.0047	0.0042
Dendate vs. RightCrusI	0.5773	0.0444	**Probt<<0.0001**	**0.0097**	0.2808	0.0306	0.0701	0.0097	0.1311	0.025
Dendate vs. RightVI	0.5212	0.0417	**Probt<<0.0001**	**0.0056**	0.7845	0.0444	0.0595	0.0069	0.3596	0.0319
Dendate vs. VERMISCRUSII	0.0111	0.0181	**0.0024**	**0.0222**	0.0564	0.0167	0.0081	0.0014	0.04	0.0181
Dendate vs. VermisIX	**0.0001**	**0.0056**	0.0355	0.0292	0.2433	0.0292	0.2522	0.0236	0.987	0.05
Dendate vs. VERMISVIIB	**0.0344**	**0.0236**	**Probt<<0.0001**	**0.0083**	0.9781	0.05	0.0663	0.0083	0.8776	0.0458
Dendate vs. VermisVIIIa	0.06	0.0264	**0.0002**	**0.0125**	0.7104	0.0417	0.0135	0.0028	0.4532	0.0361
Dendate vs. VermisX	**Probt<<0.0001**	**0.0014**	0.1121	0.0347	**0.0002**	**0.0014**	0.1478	0.0139	0.0359	0.0153
LeftCrusI vs. RightCrusI	**0.0107**	**0.0167**	**0.0071**	**0.0236**	0.199	0.025	0.2295	0.0194	0.1402	0.0278
LeftCrusI vs. RightVI	0.0215	0.0194	**0.0007**	**0.0139**	0.057	0.0181	0.1885	0.0167	**0.0007**	**0.0014**
LeftCrusI vs. VERMISCRUSII	0.9349	0.05	0.1438	0.0361	0.947	0.0486	0.03	0.0042	0.6506	0.0431
LeftCrusI vs. VermisIX	0.2342	0.0361	0.9634	0.0486	0.2314	0.0278	0.611	0.0403	**0.0049**	**0.0056**
LeftCrusI vs. VERMISVIIB	0.5684	0.0431	**0.0012**	**0.0194**	0.0463	0.0139	0.189	0.0181	0.0099	0.0097
LeftCrusI vs. VermisVIIIa	0.4069	0.0389	**0.0205**	**0.0264**	0.0217	0.0097	0.0476	0.0056	**0.0022**	**0.0028**
LeftCrusI vs. VermisX	**0.0014**	**0.0125**	**0.001**	**0.0181**	0.0483	0.0153	0.3905	0.0292	0.5078	0.0389
RightCrusI vs. RightVI	0.9037	0.0486	0.2848	0.0403	0.4573	0.0389	0.8493	0.0486	0.024	0.0139
RightCrusI vs. VERMISCRUSII	0.0332	0.0222	0.3431	0.0431	0.3012	0.0319	0.2303	0.0208	0.4123	0.0333
RightCrusI vs. VermisIX	**0.0005**	**0.0069**	**0.008**	**0.025**	0.9272	0.0472	0.4811	0.0347	0.1351	0.0264
RightCrusI vs. VERMISVIIB	0.0919	0.0292	0.2714	0.0389	0.3431	0.0361	0.7766	0.0444	0.1508	0.0292
RightCrusI vs. VermisVIIIa	0.1498	0.0333	0.9904	0.05	0.2002	0.0264	0.3201	0.025	0.0466	0.0222
RightCrusI vs. VermisX	**Probt<<0.0001**	**0.0028**	**Probt<<0.0001**	**0.0042**	**0.0027**	**0.0069**	0.7785	0.0458	0.4598	0.0375
RightVI vs. VERMISCRUSII	0.0545	0.025	0.0758	0.0333	0.1118	0.0222	0.3251	0.0264	0.0086	0.0083
RightVI vs. VermisIX	**0.0013**	**0.0097**	0.0008	0.0153	0.408	0.0375	0.395	0.0306	0.3518	0.0306
RightVI vs. VERMISVIIB	0.1347	0.0319	0.9023	0.0472	0.7943	0.0458	0.9166	0.05	0.5204	0.0403
RightVI vs. VermisVIIIa	0.2073	0.0347	0.3524	0.0444	0.559	0.0403	0.4319	0.0333	0.9365	0.0486
RightVI vs. VermisX	**Probt<<0.0001**	**0.0042**	**Probt<<0.0001**	**0.0014**	**0.0006**	**0.0042**	0.6546	0.0417	**0.0056**	**0.0069**
VERMISCRUSII vs. VermisIX	0.2744	0.0375	0.1542	0.0375	0.338	0.0347	0.076	0.0111	0.0412	0.0194
VERMISCRUSII vs. VERMISVIIB	0.6552	0.0458	0.0676	0.0319	0.0771	0.0208	0.4058	0.0319	0.0444	0.0208
VERMISCRUSII vs. VermisVIIIa	0.4942	0.0403	0.3929	0.0458	0.0402	0.0125	0.8488	0.0472	0.0129	0.0111
VERMISCRUSII vs. VermisX	**0.0042**	**0.0153**	**0.0001**	**0.0111**	0.0769	0.0194	0.1674	0.0153	0.8875	0.0472
VermisIX vs. VermisVIIIa	0.0713	0.0278	**0.0224**	**0.0278**	0.1754	0.0236	0.1147	0.0125	0.445	0.0347
VermisIX vs. VermisX	0.0225	0.0208	**0.0009**	**0.0167**	**0.0033**	**0.0083**	0.7009	0.0431	0.0371	0.0167
VERMISVIIB vs. VermisIX	0.1187	0.0306	**0.0014**	**0.0208**	0.306	0.0333	0.3745	0.0278	0.8667	0.0444
VERMISVIIB vs. VermisVIIIa	0.811	0.0472	0.3103	0.0417	0.7543	0.0431	0.5199	0.0375	0.5855	0.0417
VERMISVIIB vs. VermisX	**0.0013**	**0.0111**	**Probt<<0.0001**	**0.0028**	**0.0008**	**0.0056**	0.6062	0.0389	0.0515	0.0236
VermisVIIIa vs. VermisX	**0.0007**	**0.0083**	**Probt<<0.0001**	**0.0069**	**0.0003**	**0.0028**	0.2352	0.0222	0.0146	0.0125